PCCP

ROYAL SOCIETY OF CHEMISTRY

PAPER

View Article Online
View Journal

Cite this: DOI: 10.1039/d5cp00834d

Low-density Ag–Au nanoparticle photodeposition on TiO_2 thin film photocatalysts grown by atomic layer deposition†

Bela D. Bhuskute, ‡[a] Tuomas Tinus,‡[a] Harri Ali-Löytty, *[ab] Jesse Saari,[a] Kimmo Lahtonen [c] and Mika Valden*[a]

Heterogeneous TiO_2 photocatalysts, decorated with noble metal co-catalysts *via* photodeposition, have been recognized for their efficacy across a spectrum of photocatalytic applications. Improved performance is often attributed to either plasmonic enhancement or improved separation of photoinduced charge carriers by noble metal nanoparticles. The differentiation between the two typically co-existing mechanisms is challenging and calls for investigations using model systems in which either mechanism is suppressed. To bridge this gap, low number density ($<100\ \mu m^{-2}$) Au and Ag monometallic and bimetallic nanoparticles (NPs) were synthesized *via* photodeposition from liquid precursors on anatase titania (TiO_2) thin films fabricated by atomic layer deposition (ALD). Initiating bimetallic NP deposition with Au first created bimetallic Au-core–Ag-shell NP/TiO_2 thin film catalysts, which showed the highest activity towards photodegradation of methylene blue. Conversely, reversing the order (starting with Ag) resulted in a Au–Ag alloy/TiO_2 structure *via* a galvanic replacement reaction exhibiting bimodal particle size distributions of the Au–Ag alloy and Au alone – showing the lowest photocatalytic activity. The presence of low number density metal nanoparticles does not impact the optical absorption of TiO_2 in the UV-vis wavelength range *via* localized surface plasmon resonance (LSPR), but photocatalytic performance is improved due to the formation of a metal–semiconductor Schottky junction, which lowers recombination through spatial separation of charges. X-ray photoelectron spectroscopy results show the highest activity towards oxidation in an air atmosphere for Au-core–Ag-shell NPs/TiO_2, mirroring the results of the photocatalytic test. We conclude that the Au-core–Ag-shell is the optimal morphology for noble metal NP co-catalysts on an anatase TiO_2 support.

Received 3rd March 2025,
Accepted 15th July 2025

DOI: 10.1039/d5cp00834d

rsc.li/pccp

Introduction

Since Fujishima and Honda's groundbreaking demonstration in 1972, titanium dioxide (TiO_2) has been considered as a promising photocatalyst with versatile applications in water purification, environmental remediation and solar energy conversion.[1–5] This has positioned TiO_2 as a focal point of research aiming to combat concerns like global warming and to promote sustainable energy solutions. Despite its promising photocatalytic properties, TiO_2 faces challenges to adoption at a scale like limited response to visible light, rapid electron–hole pair recombination and a high bandgap energy hindering its efficiency in harnessing solar energy and catalysing specific reactions.[6–8]

Ongoing research aims to address these limitations by enhancing the performance of TiO_2 as a photocatalyst and broadening its applicability for sustainable energy production. Numerous strategies have been suggested, including elemental doping, integration of composite co-catalysts and designing heterostructures.[4,9–11]

In particular, the choice of gold (Au) and silver (Ag) as co-catalysts in this work can be justified by their distinctive properties and proven efficacy in photocatalysis. Silver is recognized for its catalytic properties, whereas gold is known for its high stability and efficiency in catalytic reactions.[12–15] The combination of Ag–Au bimetallic nanoparticles exhibit absorption over a wide wavelength range of visible light in the solar spectrum.[16] Additionally, the Ag–Au bimetallic system has an advantage due to comparable lattice constants (2.3/2.4 Å for the

[a] Surface Science Laboratory, Faculty of Engineering and Natural Sciences, Tampere University, FI-33014 Tampere, Finland
[b] Liquid Sun Ltd, Tekniikankatu 1, FI-33720 Tampere, Finland
[c] Faculty of Engineering and Natural Sciences, Tampere University, FI-33014 Tampere, Finland

† Electronic supplementary information (ESI) available: SI_01: Photocatalytic degradation curves and SEM analysis (PDF). See DOI: https://doi.org/10.1039/d5cp00834d

‡ These authors contributed equally.

Ag(111)/Au(111) facet).[17] Therefore, they can form bimetallic nanostructures with a variety of compositions. The incorporation of a metal on the oxide semiconductor surface like TiO_2, which forms a Schottky junction at the metal–semiconductor interface, offers a promising approach to decrease the recombination rate of photogenerated electron–hole pairs and improve photocatalytic activity.[18]

While plasmonic enhancement by such metal nanoparticles has been extensively studied for its capability to amplify light–matter interactions, the precise differentiation between the contributions of the plasmonic effect and charge transfer remains a critical barrier in the field. To address this challenge, we have fabricated model thin film photocatalysts by photodepositing Au and Ag nanoparticles (NPs) in monometallic and bimetallic configurations on anatase TiO_2 thin films fabricated by atomic layer deposition (ALD). We have recently reported similar synthesis on particulate TiO_2 showing plasmonic enhancement by metal NPs and synthesis of either core–shell or alloy Ag–Au NPs depending on the order of metal photodeposition.[19] In the presented work, we have made an attempt to transfer the similar synthesis from TiO_2 powders to TiO_2 thin films. The metal nanoparticle deposition synthesis procedure is similar, and the obtained results are consistent with those of TiO_2 powders.[19] The metal loading in the current study was intentionally kept low in order to keep the surface coverage and therefore the plasmonic effects low. Our intent is to study these NPs as co-catalysts rather than focusing solely on their plasmonic properties thus examining their influence on the photocatalytic reaction mechanism and studying how these co-catalysts work synergistically with TiO_2 to effectively enhance the photocatalytic process. By characterizing the metal NPs as co-catalysts, we aim to determine their distinct role in photocatalytic reactions such as degradation of the methylene blue dye and their influence on the overall material performance.

Experimental section

Materials

In the presented experiment, UV-vis transparent thermally stable fused quartz microscope slides (UQG Optics) in 25 mm × 50 mm rectangles were utilized as substrates for samples analysed in optical measurements and photocatalytic methylene blue (MB) degradation tests. Sb-doped n-type Si (100) wafer (Siegert Wafer) cleaved in 20 mm × 15 mm rectangles was used as a substrate for samples analysed with SEM and XPS. In order to deposit TiO_2 thin film coating on substrates using ALD, tetrakis(dimethylamido)titanium(IV) (TDMAT, an electronic grade of 99.999+%, Sigma-Aldrich) was employed as the Ti precursor, water (Milli-Q ultrapure type 1) as the O pre-cursor and Ar (99.9999%, Oy AGA Ab, Finland) as the carrier/purge gas. Gold chloride ($HAuCl_4{\cdot}3H_2O$, Sigma Aldrich, ≥99.9% trace metals basis), silver nitrate ($AgNO_3$, Sigma Aldrich, BioXtra >99% titration), methanol (VWR, ≥99.8% ACS reagent), methylene blue (MB) (Sigma Aldrich, 0.05 wt% in H_2O) and deionized (DI) water (Milli-Q ultrapure type 1) were used during the photodeposition process. All the chemicals were used without any further purification.

Fabrication of anatase TiO_2 thin films

Anatase TiO_2 thin films were fabricated according to the process described and characterized in detail earlier.[20,21] In short, prior to ALD, the silicon substrates were cleaned for 45 min by sonicating the Si(100) wafer in 99.5% EtOH, and fused quartz substrates were used after cleaning using ethanol and DI water followed by drying under nitrogen flow. ALD TiO_2 films of 30 nm were fabricated on the substrates at a growth temperature of 150 °C (636 ALD cycles) using a Picosun Sunale R200 Advanced reactor and the process was described by Saari *et al.*[22] in the previous study. Ellipsometry (Rudolph Auto EL III Ellipsometer, Rudolph Research Analytical, λ = 632.8 nm) was used to calibrate the thickness. After the deposition, the samples were annealed in ambient air using a tube furnace (Carbolite Gero) at 500 °C for 1 h to induce complete crystallization to anatase.[20,21] Samples were allowed to cool down before being utilized in subsequent steps.

Photodeposition of monometallic Au and Ag nanoparticles on ALD-grown titanium dioxide

Titanium dioxide thin films enhanced with Au nanoparticles were fabricated by the photodeposition method from liquid precursors on ALD-grown titanium dioxide. 0.1 mM gold chloride stock solution was prepared in DI water. 30 ml methanol and 20 ml DI water were taken in a 50 ml quartz round bottom flask (RBF). 6 wt% of Au, with respect to a mass of 30 nm TiO_2 thin films, from the precursor stock solution was added to this water–methanol solution. The TiO_2 coated substrate was immersed in the mixture and positioned vertically within the RBF. A magnetic stirring bar was introduced while ensuring that it did not make contact with the coated substrate. Subsequently, the RBF was sealed using a rubber septum. To remove dissolved oxygen, the solution was purged with nitrogen gas for 30 min by inserting a needle *via* a rubber septum. In addition, a second needle was inserted to expel oxygen and other gases from the reactor. After purging, the reactor containing the sample was exposed to UV irradiation using a Newport Mercury Light Source (200 W Hg arc lamp) positioned at a distance of 30 cm from the film. Throughout the purging and UV exposure procedure, the metal stock solution in the reactor was continuously stirred. Gold (Au) was photodeposited onto anatase TiO_2 films for a duration of 60 minutes. After the photodeposition, the sample was recovered from the reactor. To maintain the purity and cleanliness of the film, it was subsequently rinsed with deionized (DI) water to eliminate any surplus or unreacted chemicals, residues, or byproducts from the surface, followed by drying in nitrogen gas flow.

Similarly, Ag was photodeposited on anatase TiO_2 films by following the procedure mentioned above by adding 3.3 wt% of Ag from 0.1 mM $AgNO_3$ stock solution to a water–methanol mixture and UV exposure of 60 min. Through this methodology, Au/TiO_2 and Ag/TiO_2 films were synthesized respectively.

Photodeposition of the bimetallic Au-core–Ag-shell and Au–Ag alloy nanoparticles on anatase TiO_2 thin films

Monometallic Au-deposited ALD anatase thin films were placed into a 50 mL quartz RBF followed by the addition of 30 mL methanol and 20 mL DI water. From the 0.1 mM $AgNO_3$ stock solution, 3.3 wt% of Ag was added into the RBF. Again, the RBF is sealed with a rubber septum, purged with nitrogen and exposed to UV irradiation, following the same process as previously outlined. After 60 minutes of photodeposition, bimetallic Au-core–Ag-shell/TiO_2 thin films were retrieved, rinsed and dried as above.[19]

The Au–Ag alloy nanoparticles on anatase TiO_2 was synthesized by altering the metal deposition sequence by first placing the monometallic Ag-deposited anatase TiO_2 film in the RBF containing 30 ml methanol and 20 ml water and adding 6 wt% of Au from the 0.1 mM $HAuCl_4$ stock solution. The procedure was carried out in order to recover Au–Ag alloy/TiO_2.[19] The stoichiometry of the bimetallic samples indicated a nominal molar ratio of Au : Ag as 1 : 1.

Characterization

The optical properties of samples were characterised using a UV-vis spectrophotometer (PerkinElmer® LAMBDA 1050 UV/vis/NIR) equipped with an integrating sphere. Transmission (T) and reflectance (R) were measured for all the samples. Absorbance was then calculated using a reflection-corrected formula: $A = -\log T/(1 - R)$.

The anatase TiO_2 thin films deposited on Si wafer substrates and sensitized by metallic nanoparticles were transferred in air to the solid-state end station (SSES) at beamline FinEstBeAMS[23] (MAX IV Laboratory, Lund, Sweden). Two sample series were used: one prepared approx. 1 week before the measurement (freshly prepared samples) and one prepared 12 months before the measurement and stored in a non-sealed dark box exposed to laboratory air at Tampere University (aged samples). Photoelectron spectra (PES) were recorded under ultrahigh vacuum (UHV) conditions in the analysis chamber of SSES without further modification of the samples. Measurements were conducted under excitation by monochromatized linearly polarized synchrotron light from an elliptically polarizing undulator. A photon energy of 678 eV was used for all the presented spectra. Photoelectron energy was measured with a hemispherical electron energy analyzer (PHOIBOS 150 2D-DLD, SPECS Surface Nano Analysis GmbH) in normal emission. The data were analyzed using CasaXPS software version 2.3.25PR1.0.[24] The binding energy scale was calibrated according to Ti $2p^{4+}$ in ALD anatase TiO_2 at 459.0 eV.[22] Shirley-type backgrounds were fitted to all spectra, and spectra were normalized to enable chemical state analysis.

Laboratory selected-area XPS was performed employing a non-monochromatized DAR400 Al Kα X-ray source and an Argus hemispherical electron spectrometer (Scienta Omicron GmbH). The spectra were collected in normal emission with an analysis area of 1.54×4.09 mm^2. The surface composition was identified by analyzing the main core level photoelectron transitions. The XPS spectra were least-squares fitted using CasaXPS software with a minimum number of GL, LA, and LF line shapes to achieve the good overall fitting of the spectra. The relative atomic concentrations were calculated using Scofield photoionization cross sections and an experimentally measured the transmission function of the analyzer.

Scanning electron microscopy (SEM) (Zeiss Ultra 55, Carl Zeiss Microscopy GmbH) was used to examine the surface morphology of the films. SEM images were captured using secondary electron (SE2) mode for samples with monometallic particles and in lens mode for samples with bimetallic particles. The images were taken with a working distance of 4.7–4.9 mm and an electron high tension (EHT) of 3.00 kV.

Following the imaging process, the SEM images (representative images shown in Fig. S2 and S3, ESI†) were subsequently employed for the particle size distribution analysis using the method described in detail by Sorvali *et al.*[9] To visualize the distribution of particle sizes within the sample, the histograms were created by using the data obtained from ImageJ. Subsequently, Gaussian distributions were fitted to the histogram data to determine key parameters such as mean particle size, standard deviation and particle densities.

Photocatalytic methylene blue test

The methylene blue photodegradation test was performed according to the protocol comprehensively described by Khan *et al.*[25] An Excitation source used in the test was an Asahi Spectra MAX-350 filtered Xe lamp with a UV-vis mirror module. The source was used in three different modes with the following wavelength ranges: without further filtering, 300–600 nm with an optical power of 100 mW cm^{-2}; with a shortpass filter (Asahi Spectra XHS0400), 300–400 nm with an optical power of 20 mW cm^{-2}; and with a longpass filter (Asahi Spectra XUL0400), 400–600 nm with an optical power of 80 mW cm^{-2}.

Results and discussion

UV/vis absorption and photocatalytic tests

Fig. 1a shows the UV-vis absorption spectra of quartz substrates, substrates with 30 nm anatase TiO_2 thin films and all the synthesized mono and bimetallic composite photocatalysts. The sharp absorption edge observed in the spectra is the characteristic of anatase TiO_2 with a high degree of crystalline order as reported in our previous study.[20] Furthermore, all samples display near-identical optical properties, indicating high reproducibility of TiO_2 thin films fabrication by ALD.

In the case of metal-deposited photocatalysts, the plasmonic enhancement properties are typically achieved through sufficiently high particle number density, promoting strong interaction between neighbouring nanoparticles and facilitating localized surface plasmon resonance (LSPR) by collective oscillation of free electrons. However, as discussed in the Introduction, in our study, we deliberately opted to keep particle density low, which leads to the absence of the distinctive LSPR peak of

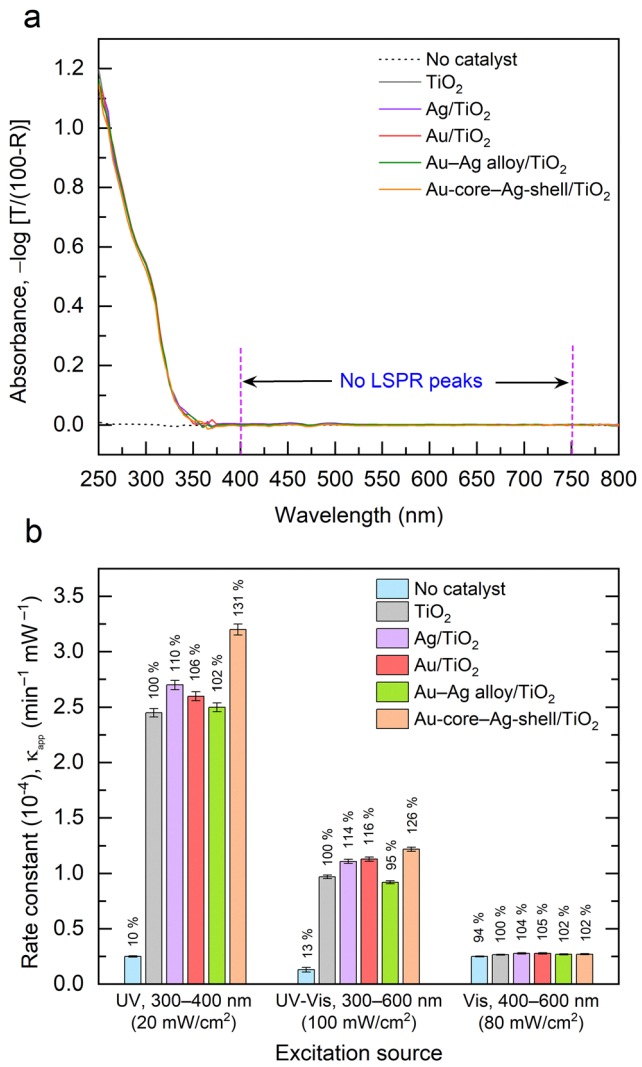

Fig. 1 (a) UV-Vis absorption spectra: bare quartz substrate, plain 30 nm thick anatase TiO_2 thin films, and Ag/TiO_2, Au/TiO_2, Au–Ag alloy/TiO_2, and Au-core–Ag-shell/TiO_2 on quartz substrates. (b) Photocatalytic degradation of MB using metal NP deposited anatase TiO_2 thin films under solar light irradiation. Error bars are derived from the MB degradation curve-fitting error and light intensity calibration error.

Ag and Au NPs within the visible range of UV-vis spectra. LSPR peaks for Ag–Au NPs would appear in the 400–750 nm range.[19]

In order to evaluate the photocatalytic activity of these photocatalyst thin films, methylene blue (MB) dye degradation experiments were conducted under three different excitation conditions: UV (300–400 nm), UV-vis (300–600 nm) and Vis (400–600 nm) excitation, with optical powers of 20 mW cm^{-2}, 100 mW cm^{-2}, and 80 mW cm^{-2} respectively. The obtained results were normalized to the excitation power used in the respective experiments and are presented in Fig. 1b (raw data presented in Fig. S1, ESI†). All the TiO_2 samples exhibited strong photocatalytic activity under UV excitation. In contrast, photocatalytic activity under only visible light excitation was insignificant and methylene blue degradation was dominated by the photolysis in the solution phase,[26] that is, the degradation rate without any catalyst. Under UV-vis excitation, relative activities were similar to UV only excitation.

To give a clearer context to the enhancement magnitude by the metal NPs in different excitation wavelength ranges, the photocatalytic activity of plain TiO_2 was considered as the 100% reference in each set of samples. Therefore, under UV excitation, Ag/TiO_2 and Au/TiO_2 exhibit enhanced activities of 110% and 106%, respectively, signifying 10% and 6% improvements over plain TiO_2. Amongst all the studied catalysts, Au-core–Ag-shell/TiO_2 films demonstrated outstanding performance with 31% enhancement in photocatalytic activity under UV excitation and 26% enhancement under UV-vis excitation compared to the plain TiO_2 film. Although Au–Ag alloy/TiO_2 had comparable metal loading to Au-core–Ag-shell/TiO_2, the sequence of deposition influenced the photocatalytic activity, leading to reduced performance for Au–Ag alloy/TiO_2 photocatalysts. This highlights the importance of the photodeposition sequence in determining the photocatalytic efficiency of photodeposited metal NP–TiO_2 catalysts.[19] It is worth noting that even monometallic Ag/TiO_2 and Au/TiO_2 depicted higher photocatalytic activity compared to bimetallic Au–Ag alloy/TiO_2. From the combination of UV-visible spectra and photocatalytic MB degradation tests, it was concluded that samples were photocatalytically active only under UV excitation. In other words, samples were not active under visible light excitation, and the observed differences are not caused by any plasmonic property. This result stands in contrast to the findings reported in our previous article[19] and by Patra *et al.*,[10] where it was observed that bimetallic Ag–Au nanoparticles photodeposited on TiO_2 significantly enhance visible light absorption across the entire visible spectrum due to strong LSPR effects. A high particle density of metallic nanoparticles is essential for inducing the LSPR effect to enhance visible light absorption. Beyond simply increasing the cross-section of interaction with the exciting light, a higher particle density also intensifies the LSPR effect through near-field resonant interactions between the neighbouring particles.[27] In this work, however, keeping the particle density low reduces the LSPR effect, allowing us to differentiate the effect of photoinduced charge carrier separation by the noble metal nanoparticles.

XPS analysis

The chemical state of the samples was investigated with synchrotron light mediated X-ray photoelectron spectroscopy (XPS). Fig. 2 presents XP spectra of the two-sample series examined in this work – freshly prepared (fabricated approx. 1 week before measurements) and aged (fabricated approx. 1 year before measurements and stored in air). Ti 2p spectra, as shown on the left in Fig. 2, are near-identical for all samples, showing a strong Ti^{4+} peak (calibrated to 459.0 eV) and a negligible amount of Ti^{3+} defect states at a binding energy (BE) of 457.2 eV, as expected for air-annealed ALD anatase films.[22] In Ag 3d and Au 4f spectra from both sample series, it is immediately apparent that the primary metallic Ag 3d (Ag $3d_{5/2}$ at 367.9 eV B.E.) and Au 4f (Au $4f_{7/2}$ at 83.7 eV B.E.) peaks are shifted to 0.3–0.4 eV lower energies than the commonly

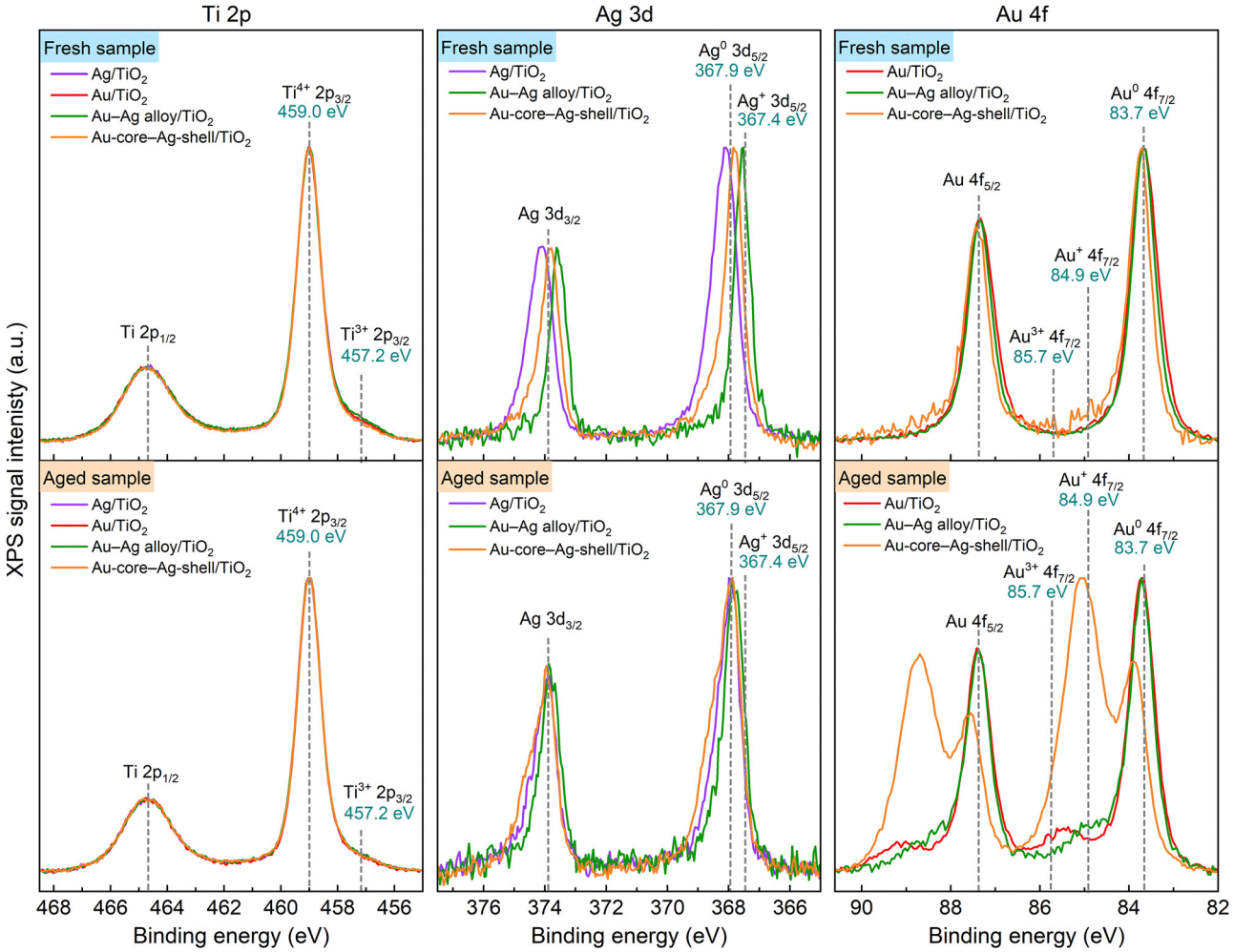

Fig. 2 Normalized Ti 2p, Ag 3d and Au 4f XP spectra of the freshly prepared sample series (above) and aged sample series (below). Spectra were recorded at a photon energy of 678 eV. Chemical state shifts in the listed binding energy values are referenced to the literature.

accepted literature values for Ag and Au in a planar (bulk) form (368.3 eV and 84.0 eV, respectively).[28] While a conclusive link to a singular cause could not be identified in this study, a number of effects that influence the binding energy of oxide-supported nanoparticles were considered. The surface core level shift due to under-coordinated atoms on the surface could play a role for Au NPs but is negligible for Ag when measuring in a normal emission configuration.[29] Differential charging effects can be excluded due to the absence of the corresponding increase in width (FWHM) of the metal peaks. Formation of a thin surface oxide layer hindering charge transfer to the semiconductor substrate and therefore uniform charging and peak shift has been hypothesized by Dikovska *et al.* for a similar material system.[30] Finally, the shift could be caused by final state effects (relaxation).[31] Generally, the existence of a shift in the binding energy of metallic Ag and Au nanoparticle peaks toward lower values than planar, with magnitude depending on the preparation method, is well-documented in the literature.[32,33]

As in our previous work on photodeposited mono- and bimetallic Ag and Au nanoparticles,[19] XP spectra in Fig. 2 point towards freshly deposited NPs being in primarily metallic phases, with no shift in Au spectra observed due to different particle morphologies. The Ag XP spectra for fresh samples have the primary Ag $3d_{5/2}$ peak at slightly varied energies in the 367.5–368.0 eV range. The binding energy shifts for different Ag oxidation states are minor[28] and can be muddled by initial and final state effects which have been discussed prior. We can, however, examine the resulting width of the peaks −0.6 to 0.7 eV for Au–Ag alloy/TiO_2 and Au-core–Ag-shell/TiO_2 samples, and 1.0 eV for Ag/TiO_2 which would indicate the metallic state and partially oxidized state, respectively. When we proceed to consider the XP spectra of the aged sample series, the contrast between samples is much more drastic. In Au 4f spectra, a metallic phase is still clearly identifiable, but an oxidized Au phase is present as well. For Au/TiO_2 and Au–Ag alloy/TiO_2 samples, a small additional peak and shoulder, respectively, are present, consistent with minor contributions from Au^{3+} and Au^{+}.[28] The most significant change is observed in the Au-core–Ag-shell/TiO_2 sample, where the oxidized phase, primarily Au^{+}, becomes dominant over the metallic. A similar change is observed in Ag 3d spectra – Au–Ag alloy/TiO_2 still presents the narrowest FWHM of 0.8 eV for the Ag $3d_{5/2}$, and

Table 1 Surface concentrations of Ag and Au on TiO_2 thin films

At%, TiO_2 bal.	Ag	Au
Ag/TiO_2	0.9	—
Au/TiO_2	—	1.5
Au–Ag alloy/TiO_2	0.7	0.6
Au-core–Ag-shell/TiO_2	1.4	1.6

Au-core–Ag-shell/TiO_2 is the widest at a FWHM of 1.0 eV. Based on these data, we believe that in Au-core–Ag-shell NPs atmospheric oxygen partially oxidizes the Ag shell and over time and oxygen diffuses to the Au core – strongly oxidizing it in turn. In the literature, formation of Au^+ species in oxide-supported nanoparticle catalysts has been tied to improved activity in photocatalytic reactions, *e.g.* low temperature CO oxidation.[34] We propose that the oxidation of these nanoparticles in an air atmosphere is related to their catalytic activity as measured in this work through methylene blue photodegradation. The reactivity to oxygen, like catalytic activity, is specific to nanoparticle morphology – oxygen molecules are not even adsorbed on planar gold surfaces.[35] Au–Ag alloy NPs show only a minimal change between the freshly prepared and aged series, and minimal enhancement of catalytic activity to methylene blue degradation over plain TiO_2 – while Au-core–Ag-shell NPs are strongly oxidized in storage and show the best enhancement of photocatalytic activity. Under photocatalytic conditions, oxidation of the nanoparticles would not occur, since Ag and Au atoms are readily reduced by photogenerated electrons but provides valuable insight into the catalytic properties of the NPs.

The surface composition of the metal-deposited samples was studied further using conventional laboratory-based XPS. Relative atomic concentrations of Ag and Au were calculated from the fitted XPS spectra, and the results are presented in Table 1.

The monometallic Ag/TiO_2 sample showed the lowest metal concentration of 0.9 at%, and bimetallic Au-core–Ag-shell/TiO_2 showed the highest total metal concentration of 3.0 at%. The differences in metal surface concentrations can reflect differences in particle sizes. Furthermore, XPS data for bimetallic nanoparticle samples show Ag and Au at near-equal amounts on the sample surface. Assuming that the nanoparticle morphology for Ag and Au with mean particle size is larger than the XPS information depth (5–10 nm), the XPS surface concentrations correspond to the surface coverage of metal NPs on TiO_2 substrates. Thus, the obtained values suggest the low surface coverage ($<3\%$) of metal NPs on TiO_2 substrates.

Particle size analysis

The particle size distribution analysis was conducted on samples after photodeposition of nanoparticles on anatase TiO_2 thin films fabricated on the silicon substrate using multiple SEM images (representative images shown in Fig. S2 and S3, ESI†). Histograms were plotted; Gaussian fitting was applied to the obtained data and is presented in Fig. 3. Also, the particle sizes, standard deviation and particle densities were calculated and are presented in Table 2. In the Ag/TiO_2 sample, the particle size for Ag was determined to be 21.7 nm with a standard deviation (SD) of 8.7 nm, while for the Au/TiO_2 sample, the particle size of Au was 13.7 nm, which was smaller than the Ag particle size with an SD of 3.9 nm. In the case of the Au-core–Ag-shell/TiO_2 sample structure, a single particle size distribution was observed with a particle size of 20.9 nm and an SD of 7.6 nm. This bigger particle size in the Au-core–Ag-shell sample than monometallic Au is justifiable due to the presence of an Au-core and Ag-shell photodeposited on top, resulting in the larger particle size than the Au monometallic sample.

In contrast, the Au–Ag alloy/TiO_2 sample exhibited two distinct particle size distributions, with peaks at 15.2 nm and 30.3 nm with SDs of 5.9 nm and 6.8 nm, respectively. For the first peak, the particle size closely resembled the particle size of the monometallic Au sample, also suggesting the presence of monometallic Au in the alloy sample. The second distribution with a larger particle size of 30.3 nm might indicate the presence of an alloy of Au and Ag in accordance with ref. 19 with the particle size larger than the monometallic Ag sample. This observation indicates the existence of two mixed particle size distributions of Au alone and Au–Ag alloy in the Au–Ag alloy/TiO_2 sample. This is corroborated by a significantly increased NP density for the Au–Ag alloy sample relative to monometallic Ag. It may further indicate that when Au is photodeposited on top of Ag NP/TiO_2 in addition to formation of Au–Ag alloy Au NPs are formed in areas of the TiO_2 substrate outside of direct proximity to Ag NPs. This is enabled by the design low number density of NPs on the surface.

The tabulated particle densities confirm the low surface coverage of these co-catalyst metal nanoparticles on anatase TiO_2 thin films. If the surface was completely covered by a close packed layer of 21 nm NPs, the corresponding density would be approx. 2620 μm^{-2}, with densities observed in this work being two orders of magnitude lower. The particle densities are also consistent with the XPS data, with the lowest metal concentration determined by XPS for Ag/TiO_2 matching here to the lowest NP density of the four analyzed samples.

Mechanism of photocatalytic degradation of MB by Au–Ag/TiO_2 thin films

In our findings, the photocatalytic activity of monometallic Ag/TiO_2 and Au/TiO_2 exceeded that of Au–Ag alloy/TiO_2 which contradicts the results obtained by Haider *et al.* and Malik *et al.* where Au–Ag alloy NPs on TiO_2 outperformed in photocatalytic activity compared to monometallic NPs.[36,37] Whereas it was found that under certain conditions, monometallic Ag/TiO_2 and Au/TiO_2 outperformed Au–Ag alloy/TiO_2.[19,38]

Based on our observations, we propose the following scheme of photocatalytic degradation of MB by low number density Au-core–Ag-shell nanoparticles decorated on the TiO_2 surface, as illustrated in Fig. 4. For high number density plasmonic metal nanoparticle-sensitized TiO_2 under combined UV-vis illumination, the main direction of electron transfer is from the excited NPs to TiO_2 – *via* hot carrier transfer (HET) and PIRET mechanisms.[39] Previous results published on the particulate

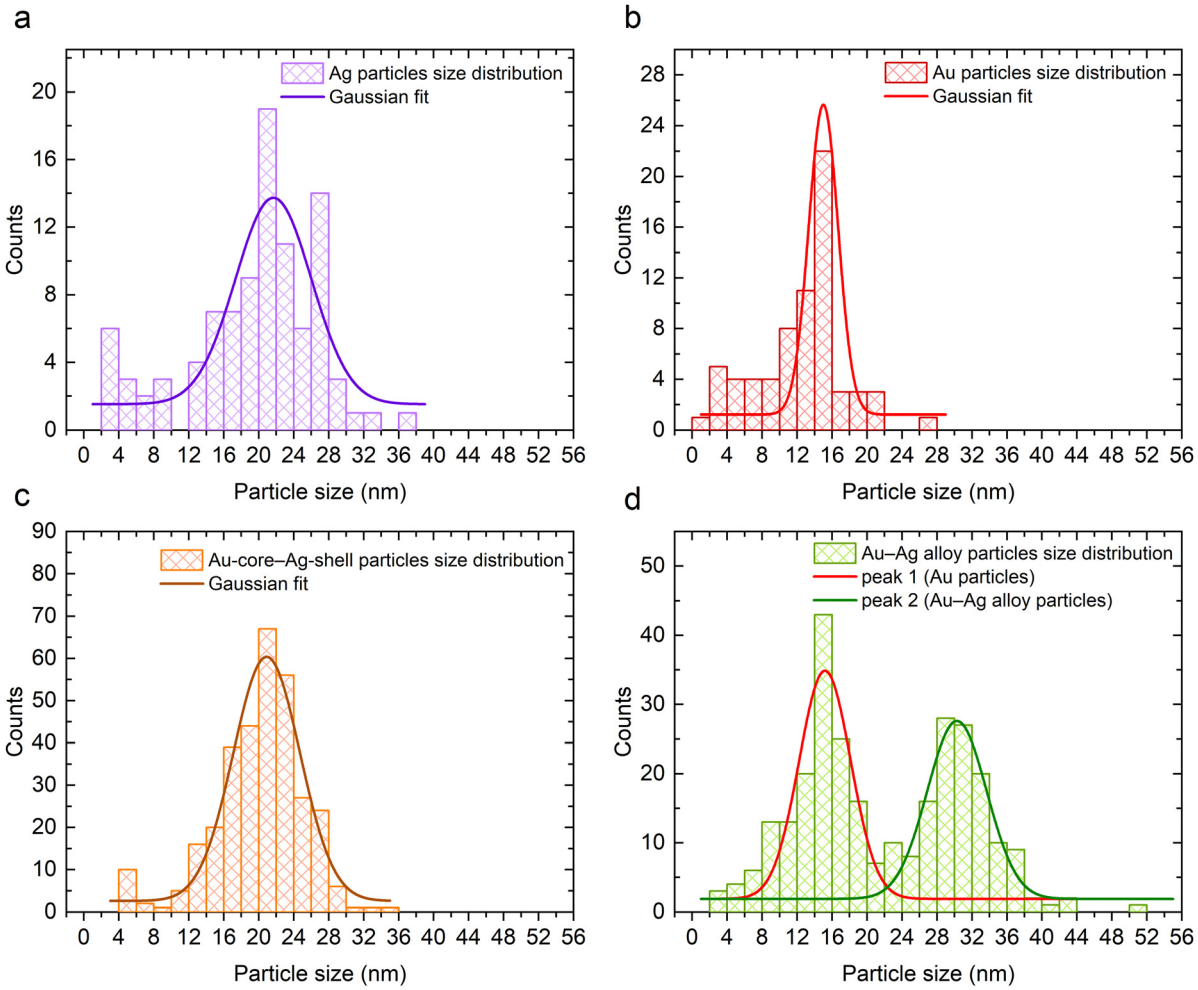

Fig. 3 Histogram of particle size distribution analysis calculated using ImageJ software. (a) Ag, (b) Au, (c) Au-core–Ag-shell and (d) Au–Ag alloy nanoparticles on ALD TiO_2 films on Si.

Table 2 Ag and Au particle size distribution analysis

Samples	Mean size (nm)	SD (nm)	Density (μm^{-2})
Ag/TiO_2	21.7	8.7	19
Au/TiO_2	13.7	3.9	65
Au–Ag alloy/TiO_2	Peak 1 15.2	5.9	53
	Peak 2 30.3	6.8	(Total)
Au-core–Ag-shell/TiO_2	20.9	7.6	34

system indicate a significant LSPR effect following the photodeposition of metal nanoparticles on TiO_2.[10,19] Under UV light irradiation during photodeposition, the white TiO_2 changed to violet-pink with Au and light orange with Ag, due to the LSPR effect. This effect enhances visible light absorption, thereby boosting the photocatalytic reaction. This leads to strong visible light absorption at 515 nm for Ag and 555 nm for Au, thus enhancing the photocatalytic activity of TiO_2.[10,19] In the low-density case, exciting light is absorbed primarily by the TiO_2 film due to density of plasmonic nanoparticles being too low to support LSPR – as demonstrated by spectrophotometry in this work. Electrons can then be transported from the TiO_2 conduction band to the nanoparticles, separating them from holes spatially and allowing for the formation of additional reactive oxygen species able to oxidize MB molecules. Such a mechanism for dye photodegradation on noble metal NP-decorated TiO_2 catalyst systems has been previously discussed in the literature,[40] but this work provides additional evidence to support its existence.

When NPs are deposited onto the TiO_2 film surface, a Schottky barrier is formed at the metal–semiconductor interface. In plasmonically active noble metal-decorated TiO_2 catalysts, it is often considered beneficial to keep the Schottky barrier height low to enhance the transfer of hot photogenerated carriers with relatively low lifetimes from the NPs to the semiconductor, boosting photocatalytic efficiency.[41] However, the increased Schottky barrier height confers benefits of its own – allowing for the improved spatial separation of charge carriers between NPs and the TiO_2 substrate, which suppresses recombination outside of their interface. This is the key for TiO_2 enhanced with low-density metal co-catalysts, such as the ones discussed in this work, since carriers are not generated by plasmonic light absorption in metal NPs and recombination is one of the strongest factors limiting efficiency.

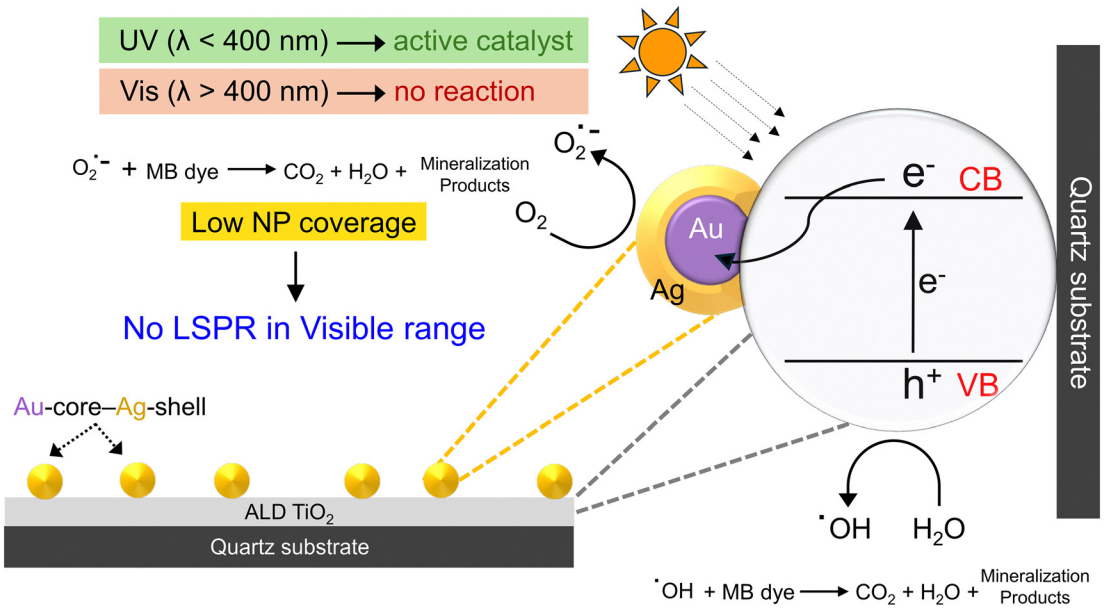

Fig. 4 Schematic representation of photocatalytic methylene blue degradation activity by Au-core–Ag-shell/TiO_2 photocatalyst films when NP coverage is low enough to prevent LSPR induced visible light absorption.

The height of the Schottky barrier is influenced by a number of factors – the primary of which is the nature of the semiconductor and metal involved, but also the metal nanoparticle size and shape.[41,42] For Ag and Au metals, the work functions are approx. 4.7 eV and 5.4 eV, respectively, while for TiO_2 the work function is 4.6–4.7 eV.[18,43] The larger work function difference for the Au–TiO_2 junction results in a higher Schottky barrier height than for the Ag–TiO_2 junction, and therefore improved charge separation. In the case of Au-core–Ag-shell NPs, it is crucial to note that due to the photodeposition sequence Au is in galvanic contact with the TiO_2 substrate, allowing for the improved suppression of recombination over Ag and Au–Ag alloy nanoparticles and also over Au-core–Ag-shell NPs synthesized by other methods than photodeposition. In comparison, when Au-core–Ag-shell NPs are synthesized in the liquid phase and subsequently coated on TiO_2, the Ag–TiO_2 junction is formed instead. Therefore, manufacturing of such hybrid Au-core–Ag-shell NPs by photodeposition allows for the improved suppression of recombination over Ag and Au–Ag alloy nanoparticles and also over Au-core–Ag-shell NPs synthesized by alternative methods. To sum up, the Schottky barrier formation at the interface between the Au–Ag nanoparticles and TiO_2 contributes to the improved photocatalytic activity, showcasing the performance of the Au-core–Ag-shell/TiO_2 system manufactured using photodeposition.

The research findings presented hereby indicate that the Au-core–Ag-shell NPs on TiO_2 exhibit superior photocatalytic methylene blue degradation performance compared to the Au–Ag alloy configuration. The Au-core–Ag-shell NPs evidenced also distinct activity towards oxidation in air that highlights exceptional catalytic activity of this bimetallic co-catalyst. Nonetheless, the enduring stability of the Ag-shell remains a significant concern due to its susceptibility to photoanodic dissolution and cathodic redeposition.[44] It is postulated that the presence of the Au-core could enhance the stability of the Ag-shell by facilitating the redeposition of dissolved Ag ions. An alternative approach for improving stability explored in this work entails the alloying of Ag with Au.[19] Another approach that could be explored in the future is deposition of additional ultrathin ALD TiO_2 layers over the NPs, which could stabilise them against dissolution without impacting photocatalytic activity.

Conclusions

The findings outlined in this study describe the use of the photodeposition technique with liquid precursors to successfully deposit Ag and Au noble metal nanoparticles onto photocatalytically active TiO_2 thin film substrates. The bimetallic samples exhibited an equal concentration of Au and Ag metals. The order of photodeposition of these metal co-catalysts was determined to have a notable effect on morphology and the overall photocatalytic efficiency of bimetallic Ag–Au/TiO_2 thin films.

In the Au-core–Ag-shell/TiO_2 photocatalyst film, the increase of particle size relative to that of monometallic Au from 14 ± 4 nm to 21 ± 8 nm is in accordance with expected outcomes considering the morphology. In contrast, in the Au–Ag alloy/TiO_2 sample, a bimodal particle size distribution of monometallic Au and Au–Ag alloy morphology was obtained *via* SEM imaging-based particle size distribution analysis.

The strategic low-surface coverage photodeposition of noble metal nanoparticles on TiO_2 does not show increased light absorption but still demonstrates a significant enhancement of photocatalytic activity. This enhancement follows from the

improvement in photogenerated charge separation by the Schottky effect leading to suppression of recombination. The Schottky barrier height is higher for the Au/TiO_2 junction than Ag/TiO_2 due to the higher difference in work functions, resulting in lower recombination. Ultimately, this leads to improved photocatalytic performance in methylene blue degradation compared to the as-deposited pure TiO_2 photocatalyst, which is demonstrated in this work. The mechanism of charge transfer discussed here supports the observed order of catalytic enhancement by the nanoparticles – Au–Ag alloy/TiO_2 < monometallic Ag/Au/TiO_2 < Au-core–Ag-shell/TiO_2. These conclusions are further supported by the results of XPS surface analysis, which shows that over extended periods of exposure to ambient air Au-core–Ag-shell NPs show the highest activity towards oxidation, and Au–Ag alloy NPs show the lowest – mirroring the results of the methylene blue degradation test. Based on this, we conclude that the Au-core–Ag-shell is the optimal morphology for noble metal NP co-catalysts on anatase TiO_2 support.

Author contributions

BDB designed the synthesis of the metal deposition, obtained the UV-vis spectra and SEM data, and performed the MB photodegradation measurements and particle size analysis. TT performed the synchrotron light mediated X-ray photoelectron spectroscopy (XPS) measurements. BDB and TT wrote the initial draft. JS fabricated all the ALD TiO_2 thin films used in this work. Metal percentage analysis using XPS was done by KL. All authors have given approval to the final version of the manuscript.

Conflicts of interest

There are no conflicts to declare.

Data availability

The data supporting this article have been included in the article figures in whole.

Acknowledgements

BDB thanks the EDUFI fellowship, the Jenny and Antti Wihuri Foundation (HA postdoc homing grant), the Fortum and Neste Foundation, the Finnish Foundation for Technology Promotion and the Emil Aaltosen Säätiö for research and incentive grants. TT thanks the Academy of Finland nSTAR project (decision no. 339545) and the Jenny and Antti Wihuri Foundation for financial support. JS was supported by the Vilho, Yrjö, and Kalle Väisälä Foundation of the Finnish Academy of Science and Letters. This work was supported by the Jane and Aatos Erkko Foundation (Project ''Solar Fuels Synthesis''). This work is a part of the Academy of Finland Flagship Programme, Photonics Research and Innovation (PREIN) (decision number 320165). The authors thank Muhammad Zubair for his continuous support and contribution for the scanning electron microscopy (SEM) imaging. SEM work made use of Tampere Microscopy Center facilities at Tampere University. The authors thank Markku Hannula and Lauri Palmolahti for their support and advice on synchrotron-based XPS measurements. The authors acknowledge MAX IV Laboratory for time on Beamline FinEst-BeAMS under Proposal 20230292. Research conducted at MAX IV, a Swedish national user facility, is supported by the Swedish Research council under contract 2018-07152, the Swedish Governmental Agency for Innovation Systems under contract 2018-04969, and Formas under contract 2019-02496.

Notes and references

1 A. Fujishima and K. Honda, *Nature*, 1972, **238**, 37–38.
2 K. K. Patra, B. D. Bhuskute and C. S. Gopinath, *Sci. Rep.*, 2017, **7**, 6515.
3 U. Alam, M. Fleisch, I. Kretschmer, D. Bahnemann and M. Muneer, *Appl. Catal., B*, 2017, **218**, 758–769.
4 S. Veziroglu, A.-L. Obermann, M. Ullrich, M. Hussain, M. Kamp, L. Kienle, T. Leißner, H.-G. Rubahn, O. Polonskyi, T. Strunskus, J. Fiutowski, M. Es-Souni, J. Adam, F. Faupel and O. C. Aktas, *ACS Appl. Mater. Interfaces*, 2020, **12**, 14983–14992.
5 A. Kumar, P. Choudhary, A. Kumar, P. H. C. Camargo and V. Krishnan, *Small*, 2022, **18**, 2101638.
6 in *Design of Advanced Photocatalytic Materials for Energy and Environmental Applications*, ed. J. M. Coronado, F. Fresno, M. D. Hernández-Alonso and R. Portela, Springer, London, 2013.
7 J. Schneider, M. Matsuoka, M. Takeuchi, J. Zhang, Y. Horiuchi, M. Anpo and D. W. Bahnemann, *Chem. Rev.*, 2014, **114**, 9919–9986.
8 B. Ohtani, *Catalysts*, 2013, **3**, 942–953.
9 M. Sorvali, T. Tinus, J. Thamby, M. Honkanen, H. Ali-Löytty, A. Charmforoushan, M. Valden, J. J. Saarinen and J. M. Mäkelä, *Mater. Des.*, 2024, **239**, 112800.
10 K. K. Patra and C. S. Gopinath, *ChemCatChem*, 2016, **8**, 3294–3311.
11 H. Ren, P. Koshy, F. Cao and C. C. Sorrell, *Inorg. Chem.*, 2016, **55**, 8071–8081.
12 H. Chakhtouna, H. Benzeid, N. Zari, A. el kacem Qaiss and R. Bouhfid, *Environ. Sci. Pollut. Res.*, 2021, **28**, 44638–44666.
13 D. A. Panayotov, A. I. Frenkel and J. R. Morris, *ACS Energy Lett.*, 2017, **2**, 1223–1231.
14 Y.-H. Li, J.-Y. Li and Y.-J. Xu, *EnergyChem*, 2021, **3**, 100047.
15 R. Kavitha and S. G. Kumar, *Chem. Pap.*, 2020, **74**, 717–756.
16 L. M. Liz-Marzán, *Langmuir*, 2006, **22**, 32–41.
17 X. Hong, D. Wang, S. Cai, H. Rong and Y. Li, *J. Am. Chem. Soc.*, 2012, **134**, 18165–18168.
18 M. R. Khan, T. W. Chuan, A. Yousuf, M. N. K. Chowdhury and C. K. Cheng, *Catal. Sci. Technol.*, 2015, **5**, 2522–2531.
19 B. D. Bhuskute, H. Ali-Löytty, M. Honkanen, T. Salminen and M. Valden, *Nanoscale Adv.*, 2022, **4**, 4335–4343.
20 R. Khan, H. Ali-Löytty, J. Saari, M. Valden, A. Tukiainen, K. Lahtonen and N. V. Tkachenko, *Nanomaterials*, 2020, **10**, 1567.

21 B. D. Bhuskute, H. Ali-Löytty, J. Saari, A. Tukiainen and M. Valden, *ACS Appl. Eng. Mater.*, 2024, **2**, 2278–2284.
22 J. Saari, H. Ali-Löytty, M. M. Kauppinen, M. Hannula, R. Khan, K. Lahtonen, L. Palmolahti, A. Tukiainen, H. Grönbeck, N. V. Tkachenko and M. Valden, *J. Phys. Chem. C*, 2022, **126**, 4542–4554.
23 W. Wang, A. Kivimäki, K. Chernenko, R. Pärna, T. Käämbre, E. Kukk, K. Kokko, M. Valden, M. Hirsimäki, M. Kirm and M. Huttula, *J. Phys.: Conf. Ser.*, 2022, **2380**, 012048.
24 N. Fairley, V. Fernandez, M. Richard-Plouet, C. Guillot-Deudon, J. Walton, E. Smith, D. Flahaut, M. Greiner, M. Biesinger, S. Tougaard, D. Morgan and J. Baltrusaitis, *Appl. Surf. Sci. Adv.*, 2021, **5**, 100112.
25 R. Khan, H. Ali-Löytty, A. Tukiainen and N. V. Tkachenko, *Phys. Chem. Chem. Phys.*, 2021, **23**, 17672–17682.
26 T. Soltani and M. H. Entezari, *J. Mol. Catal. A: Chem.*, 2013, **377**, 197–203.
27 P. K. Jain and M. A. El-Sayed, *Chem. Phys. Lett.*, 2010, **487**, 153–164.
28 NIST X-ray Photoelectron Spectroscopy Database, NIST Standard Reference Database Number 20, DOI: **10.18434/T4T88K**, (retrieved August 8, 2024).
29 P. H. Citrin, G. K. Wertheim and Y. Baer, *Phys. Rev. Lett.*, 1978, **41**, 1425–1428.
30 A. O. Dikovska, M. T. Alexandrov, G. B. Atanasova, N. T. Tsankov and P. K. Stefanov, *Appl. Phys. A: Mater. Sci. Process.*, 2013, **113**, 83–88.
31 Y. Kitsudo, A. Iwamoto, H. Matsumoto, K. Mitsuhara, T. Nishimura, M. Takizawa, T. Akita, Y. Maeda and Y. Kido, *Surf. Sci.*, 2009, **603**, 2108–2114.
32 J. Radnik, C. Mohr and P. Claus, *Phys. Chem. Chem. Phys.*, 2003, **5**, 172–177.
33 M. Schnippering, M. Carrara, A. Foelske, R. Kötz and D. J. Fermín, *Phys. Chem. Chem. Phys.*, 2007, **9**, 725–730.
34 M. P. Casaletto, A. Longo, A. Martorana, A. Prestianni and A. M. Venezia, *Surf. Interface Anal.*, 2006, **38**, 215–218.
35 M. Haruta, *Catal. Today*, 1997, **36**, 153–166.
36 R. S. Haider, S. Wang, Y. Gao, A. S. Malik, N. Ta, H. Li, B. Zeng, M. Dupuis, F. Fan and C. Li, *Nano Energy*, 2021, **87**, 106189.
37 A. S. Malik, T. Liu, M. Rittiruam, T. Saelee, J. L. F. Da Silva, S. Praserthdam and P. Praserthdam, *Sci. Rep.*, 2022, **12**, 2604.
38 G. L. Chiarello, M. H. Aguirre and E. Selli, *J. Catal.*, 2010, **273**, 182–190.
39 S. K. Cushing, J. Li, J. Bright, B. T. Yost, P. Zheng, A. D. Bristow and N. Wu, *J. Phys. Chem. C*, 2015, **119**, 16239–16244.
40 J. Li, Suyoulema, W. Wang and Sarina, *Solid State Sci.*, 2009, **11**, 2037–2043.
41 G. Žerjav, M. Roškarič, J. Zavašnik, J. Kovač and A. Pintar, *Appl. Surf. Sci.*, 2022, **579**, 152196.
42 S. Y. Moon, H. C. Song, E. H. Gwag, I. I. Nedrygailov, C. Lee, J. J. Kim, W. H. Doh and J. Y. Park, *Nanoscale*, 2018, **10**, 22180–22188.
43 J. Hölzl, F. K. Schulte and H. Wagner, *Work Functions of Metals, in Solid Surface Physics*, Springer-Verlag Berlin Heidelberg, 1979.
44 K. Matsubara, K. L. Kelly, N. Sakai and T. Tatsuma, *Phys. Chem. Chem. Phys.*, 2008, **10**, 2263–2269.

